The Mechanisms and Temperature Dependence of Superlattice Stacking Fault Formation in the Single-Crystal Superalloy PWA 1480

WALTER W. MILLIGAN and STEPHEN D. ANTOLOVICH

Deformation microstructures in PWA 1480 nickel-base superalloy single crystals were studied in the range of 20 °C to 1100 °C. Similar to previous investigations, superlattice stacking faults were observed after slow strain rate deformation at temperatures between 700 °C and 950 °C. Unlike previous studies, a high density of superlattice stacking faults was observed after deformation at 200 °C and below. The mechanisms of fault formation in the two temperature regimes were different. In the range of 700 °C to 950 °C, single isolated superlattice-intrinsic stacking faults (SISFs) were produced by the decomposition of an $a/2\langle 110\rangle$ matrix dislocation in the γ/γ' interface. The $a/3\langle 112\rangle$ partial shears the particle, while the $a/6\langle 112\rangle$ Shockley remains in the interface. At 200 °C and below, a high density of faults was produced on closely spaced parallel planes. The most common feature after deformation in this range is the faulted loop, which is most often observed to be a superlattice-extrinsic stacking fault (SESF). These low-temperature faults, along with their temperature dependence, were quite similar to those observed in single-phase $L1_2$ materials. The available evidence suggests that the low-temperature faults were produced by the dissociation of an $a\langle 110\rangle$ unit superdislocation into a pair of $a/3\langle 112\rangle$ partials. The temperature dependence of the faulting (at low temperatures) was modeled by linear isotropic elasticity, and the results suggest that the SISF energy increases significantly from 20 °C to 400 °C. Multiplanar, overlapping superlattice faults were analyzed with respect to bond violations. This analysis suggested that an antiphase boundary (APB) on top of an SISF has a very high fault energy, similar to that of the complex stacking fault. Therefore, the presence of SISF loops on glide planes promotes further dissociation by the SISF scheme instead of the APB scheme and explains the high density of SESFs and microtwins observed in the deformation structures.

I. INTRODUCTION

PWA 1480 is a single-crystal nickel-base superalloy with well-documented microstructures and mechanical properties.[1,2] In an earlier communication,[3] the authors reported observing a surprisingly high density of superlattice stacking faults after low-temperature deformation and noted a relationship between the temperature dependence of these faults and the unique mechanical behavior of this alloy.[3] Since it was apparent that the faults played a major role in controlling the strength of the alloy, a detailed study of the faults and the mechanisms of fault formation was undertaken. In this article, the temperature dependence of these faults and the associated bounding partials are analyzed in detail, and in a forthcoming article, the relationships between the faults and the mechanical properties will be modeled.

In the $L1_2$ lattice, the $a\langle 110\rangle$ unit superdislocation can dissociate by a number of well-known mechanisms. Three of these dissociations are particularly relevant to the present work. The dissociation which is most commonly observed in superalloys is that which creates an antiphase boundary (APB). If the precursor superdislocation is in the primary octahedral slip system, the dissociation on the (111) plane is as follows:

$$a[\bar{1}01] \rightarrow \frac{a}{2}[\bar{1}01] + \text{APB} + \frac{a}{2}[\bar{1}01] \qquad [1]$$

The $a/2\langle 110\rangle$ partials may further dissociate into Shockleys if the complex stacking fault (CSF) energy is not too high. Alternatively, the $a[\bar{1}01]$ superdislocation may dissociate by the following reaction, creating a superlattice-intrinsic stacking fault (SISF) instead of an APB:

$$a[\bar{1}01] \rightarrow \frac{a}{3}[\bar{2}11] + \text{SISF} + \frac{a}{3}[\bar{1}\bar{1}2] \qquad [2]$$

The $a/3\langle 112\rangle$ partials may further dissociate by a number of schemes. Finally, if the dissociation occurs *via* Reaction [1], the resultant $a/2\langle 110\rangle$ partial can dissociate by the following reaction instead of the Shockley reaction, yielding an SISF instead of a CSF:

$$\frac{a}{2}[\bar{1}01] \rightarrow \frac{a}{3}[\bar{2}11] + \text{SISF} + \frac{a}{6}[1\bar{2}1] \qquad [3]$$

Note that a dissociation *via* Reaction [3] will result in an SISF adjacent to an APB.

WALTER W. MILLIGAN, Assistant Professor, is with the Department of Metallurgical and Materials Engineering, Michigan Technological University, Houghton, MI 49931. STEPHEN D. ANTOLOVICH, Professor and Director, is with the School of Materials Engineering, Georgia Institute of Technology, Atlanta, GA 30332-0245.

Manuscript submitted October 30, 1990.

II. EXPERIMENTAL PROCEDURES

As part of a large project,[4] a variety of mechanical tests (tension, creep, fatigue) were conducted on ⟨001⟩ and ⟨123⟩ oriented single crystals in the temperature range from 20 °C to 1100 °C. For the tensile and fatigue tests, two strain rates were used, 8.33×10^{-5} s^{-1} (0.5 pct/min) and 8.33×10^{-3} s^{-1} (50 pct/min). Thin foils were prepared by electropolishing discs in a solution of 5 pct perchloric acid, 35 pct butyl cellusolve, and 60 pct methanol at −25 °C and 9 to 12 V. Foils were studied on three different JEOL microscopes: a 100C operating at 100 kV, a 2000FX operating at 200 kV, and a 4000FX operating at 400 kV. Dislocations and faults were analyzed by standard two-beam techniques and by g-3g weak-beam dark-field techniques. In order to verify that the observed structures were representative and reproducible, approximately 20 foils were studied from four different specimens which had been deformed at 20 °C, and a minimum of five foils per temperature were studied from specimens which had been deformed at 200 °C, 400 °C, 600 °C, and 700 °C to 1100 °C.

III. DEFORMATION MICROSTRUCTURES

As found previously,[1] the deformation behavior of PWA 1480 can be divided into two temperature regimes: at high temperatures (above 815 °C to 950 °C, depending on $\dot{\varepsilon}$), deformation occurs primarily by dislocation bypass of the γ' precipitates; at lower temperatures, deformation occurs by dislocation shearing of the γ'. This was confirmed to be valid for both monotonic and cyclic deformation.

The behavior of the alloy in the γ' shearing regime can be further divided based on the temperature dependence of superlattice stacking fault formation. After deformation at intermediate temperatures (700 °C to 900 °C), occasional single stacking faults were observed. (These will be referred to as "high-T faults" for the remainder of this article.) After deformation at low temperatures (200 °C and below), high densities of overlapping stacking fault loops were observed. (These will be referred to as "low-T faults.") The character of the faults and the mechanisms of formation appear to be different in the two temperature regimes.

A. *High-T Faults*

After low $\dot{\varepsilon}$ deformation at temperatures between 700 °C and 900 °C, large superlattice-intrinsic stacking faults (SISFs) were observed which frequently traversed entire γ' precipitates. These faults were reported in an earlier phase of this work[1] and have been observed in similar alloys and studied by other investigators. Caron *et al.*[5] have shown by high-resolution weak-beam microscopy that these faults form at 760 °C in CMSX-2 by the decomposition of an interfacial $a/2\langle 110\rangle$ matrix dislocation *via* Reaction [3]. The $a/3\langle 112\rangle$ partial enters the precipitate, creating an SISF, while the $a/6\langle 112\rangle$ partial remains in the interface, pinned by the high-energy APB that would be created if it entered the precipitate. Bonnet and Ati,[6] using elegant image simulations, have verified that this is the predominant mechanism of fault formation during creep of CMSX-2 in this temperature regime. This mechanism has also been observed in a similar superalloy, AM1, which was deformed in the same temperature regime.[7]

A typical micrograph from PWA 1480 which was deformed in this temperature regime is shown in Figure 1. Standard two-beam techniques were used to determine the nature of the fault and the directions of the Burgers vectors of all of the partials (except the interfacial partial). The observations were compatible with the results mentioned above,[5,6] so no further work was conducted. It is concluded that the high-T faults in PWA 1480 form by the decomposition of a single $a/2\langle 110\rangle$ matrix dislocation in the γ/γ' interface, just as in CMSX-2 and AM1. This was true after both monotonic and cyclic deformation.

B. *Low-T Faults*

In contrast to the single, isolated SISFs observed after high-temperature deformation, a high density of faults was observed after deformation at 20 °C and 200 °C. These faults were most often observed as loops, as shown in Figure 2, from a specimen which had been deformed 0.25 pct in tension at 20 °C. Deformation at low temperatures is heterogeneous and is concentrated in planar slipbands. Therefore, areas like the one shown in Figure 2 are difficult to find after small plastic strains; most foils resemble the as-received material. It is possible to increase the homogeneity of the deformation structures by conducting tensile tests to large plastic

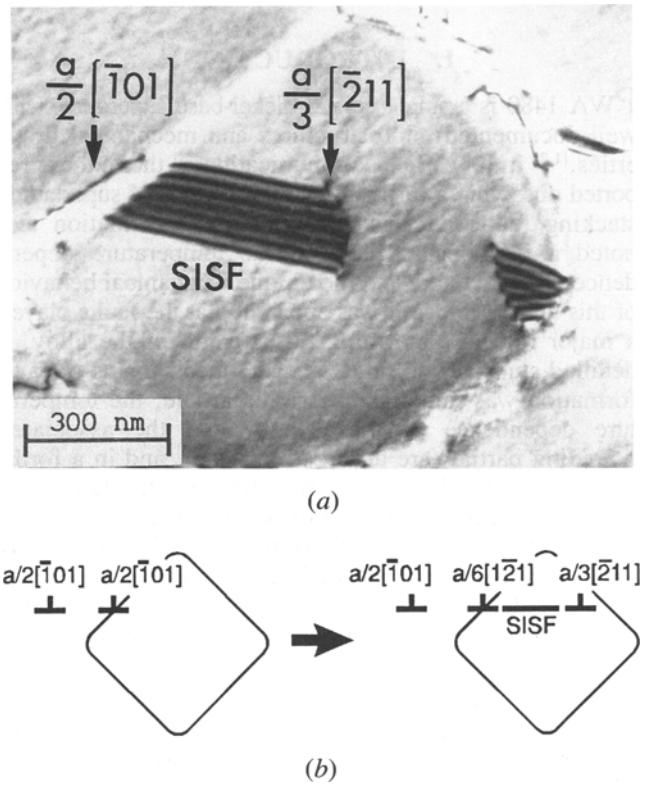

Fig. 1—Isolated SISFs after 0.26 pct plastic strain at 760 °C, $\dot{\varepsilon}$ = 0.5 pct/min: (*a*) bright-field micrograph, **g** = ⟨200⟩; (*b*) schematic diagram illustrating the dislocation reaction which probably occurred in the interface.

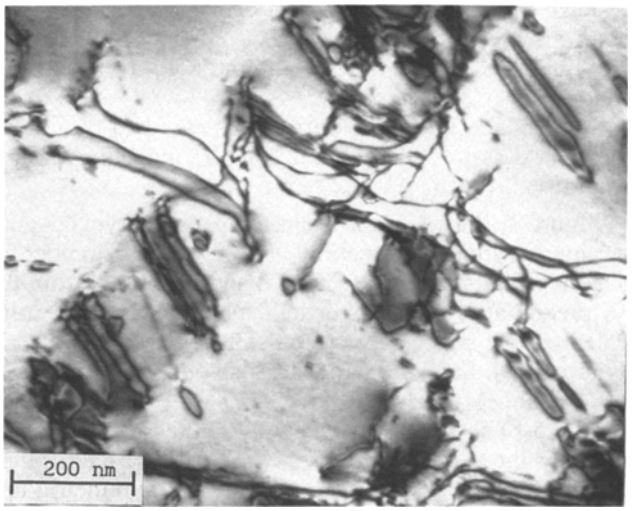

Fig. 2—Faulted loops after 0.25 pct plastic strain in tension at 20 °C, $\dot{\epsilon}$ = 0.5 pct/min, **g** = ⟨200⟩.

strains. This is not without its dangers, as the defect densities increase and the dominant deformation mechanisms can change as a function of plastic strain.[1] Another technique for improving the homogeneity of deformation (and therefore the chances of finding a representative thin area) is to impose several cycles of reversed deformation. This was found to significantly increase the likelihood of finding faults in any foil. Although the increase in fault density may be due to a change in deformation mechanism upon a load reversal, it is more likely due to the changes in degree of homogeneity. Faults and faulted loops were observed after both types of deformation, but the reproducibility of structures was greatly improved by studying specimens which had been subjected to several cycles of reversed deformation. Therefore, the majority of the structures studied in this article were produced by imposing several cycles of deformation at small plastic strain ranges.

1. *The character of the faults*

The observation of faulted loops is not consistent with the deformation mechanisms which produced the high-T faults. Therefore, a detailed study was undertaken to determine the dislocation reaction and the deformation mechanism which produced the low-T faults.

Figure 3(a) shows a typical structure after deformation at 20 °C and illustrates two key points: first, the occurrence of faulted loops within the γ' is confirmed; and second, there are a number of $a/2\langle 110\rangle$ pairs (denoted by arrows) in the matrix channels between the precipitates. Tilting experiments, along with rigorous analyses of fault vectors, Burgers vectors, and line directions, revealed that all of the faults and most of the dislocations seen in Figure 3(a) lie on the primary {111} slip planes; the dislocation pairs in the matrix channels were determined to be nearly screw, with Burgers vectors parallel to the primary ⟨110⟩ slip vector. Figure 3(b) is a micrograph of the same area as seen in Figure 3(a) with the primary slip plane edge-on, and demonstrates strikingly the planar nature of structure. This figure also shows that the matrix pairs are probably in the same slipbands that contain the faulted loops within the precipitates. All of

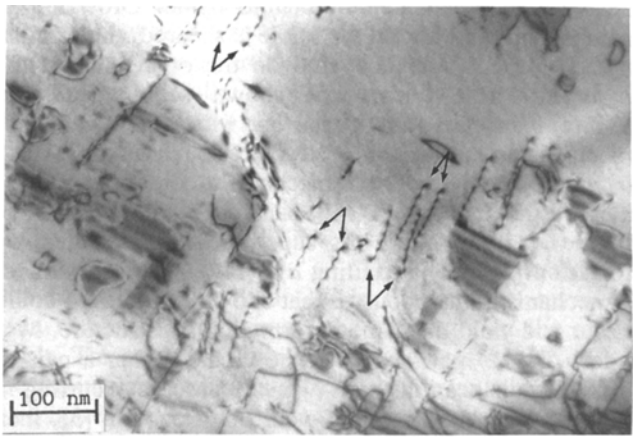

(*a*)

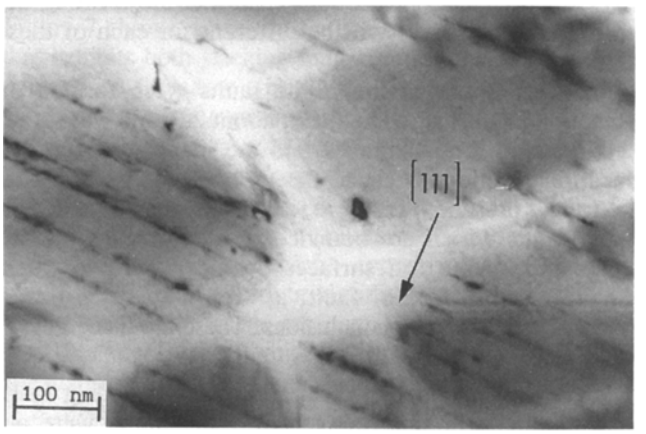

(*b*)

Fig. 3—Substructure after 6 cycles of fully reversed deformation at 20 °C, $\Delta\gamma_p$ = 0.11 pct, $\dot{\epsilon}$ = 50 pct/min: (*a*) bright-field micrograph showing faults and faulted loops in the precipitate and matrix pairs (arrows) between the precipitates, **g** = ⟨200⟩; (*b*) edge-on bright-field micrograph of the same area, showing the planar nature of the structure, **g** = ⟨111⟩.

these observations suggest a deformation mechanism in which the precipitates are sheared by dislocations with a net $a\langle 110\rangle$ Burgers vector that leaves faulted loops behind as deformation debris.

It is easy to envisage at least one deformation mechanism that could produce the structures shown in Figure 3. The $a/2\langle 110\rangle$ matrix pairs could combine to form an $a\langle 110\rangle$ superdislocation at the interface, then enter the particle. Once inside the γ', the $a\langle 110\rangle$ is free to dissociate. If the SISF energy is low compared to the APB energy, the $a\langle 110\rangle$ may dissociate *via* Reaction [2], thus producing an SISF and two $a/3\langle 112\rangle$ partials. (Note that the SISF dissociation need not occur over the entire length of the dissociation; only a local dissociation is required.) Now, if the trailing partial becomes pinned,*

*A natural question which arises is why the trailing partial should be pinned while the leading partial is mobile. This is an open question. However, as discussed in Section IV–A, a similar mechanism has been often proposed in single-phase $L1_2$ materials. Additionally, as discussed in Section IV–C, there is ample evidence that neither the leading nor the trailing $a/3\langle 112\rangle$ partial is very mobile at low temperatures.

an SISF loop can be left behind by an Orowan-type mechanism, and after the particle is sheared, the original $a/2\langle 110\rangle$ pairs are recovered on the other side of the particle. These events are shown schematically in Figure 4 and are fully consistent with Figure 3. Other mechanisms may produce structures such as those seen in Figure 3. One possible mechanism could occur when the γ' is sheared by $a/2\langle 110\rangle$ pairs connected by an APB; if the trailing $a/2\langle 110\rangle$ superpartial dissociates by Reaction [3] and its trailing $a/3\langle 112\rangle$ becomes pinned, a mechanism analogous to that shown in Figure 4 could occur and yield the same deformation substructure. Mobile $a/3\langle 112\rangle$ pairs can also be created from a pair of $a/2\langle 110\rangle$ dislocations by a two-step process occurring in the interface; the first step would be Reaction [3], then the interfacial Shockley could combine with the trailing $a/2\langle 110\rangle$ to form the glissile trailing $a/3\langle 112\rangle$. However, the dislocation reactions (and the rate-limiting deformation processes) will be different for each of these three schemes.

In order to determine if the faults were formed by Reaction [2] or [3] (or neither), about 25 foils were studied. Faulted loops cannot yield the identity of the dislocation reaction, because the reactant dislocations are no longer present. Therefore, it is necessary to study isolated faults which are bounded by dislocations on two sides and by the foil surfaces on the other two sides. Studies of this type of fault, as well as general observations, led to several conclusions. These are listed below, then discussed in detail individually.

(1) The vast majority of dislocation pairs bounding faults had parallel Burgers vectors (*i.e.*, the faults were actually truncated loops).
(2) 47 out of 53 truncated loops studied were superlattice-extrinsic stacking faults (SESFs), although SISFs and residual contrast (indicating three overlapping SISFs) were also observed.
(3) Stacking faults were commonly observed in the matrix.
(4) Often, the bounding partials appeared to be pinned at several points along their length, indicating a low mobility.

Figure 5 shows weak-beam images of typical substructures after deformation at 200 °C. A number of stacking faults are visible, and many of those within the γ' precipitates are loops or half-loops which were truncated on one side by electropolishing [marked by "L" in Figure 5(a)]. Stacking faults are also observed in the matrix channels (marked by "M" in Figure 5(a)). Figure 5(b) shows another heavily faulted area which illustrates the low mobility of the $a/3\langle 112\rangle$ partials. Many of the loops (marked by arrows) are not symmetric and appear to be pinned at several points along their perimeter. This was observed in every foil studied and is readily seen in Figures 3 and 5 through 7.

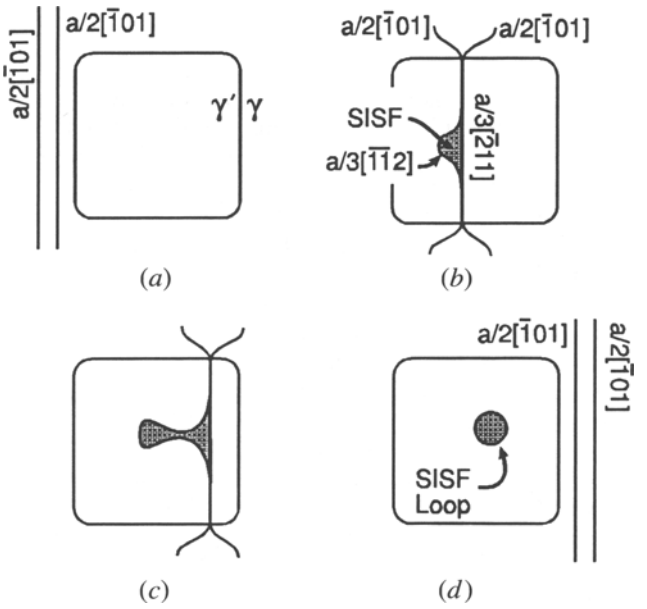

Fig. 4—Proposed model of a deformation process which leaves faulted SISF loops in the precipitate and $a/2\langle 110\rangle$ pairs in the matrix, as seen in Fig. 3. Note that the SISF dissociation does not need to occur over the entire length of the dislocation.

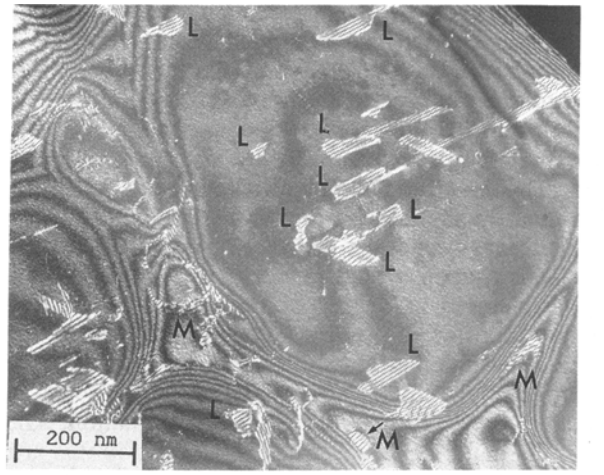

(a)

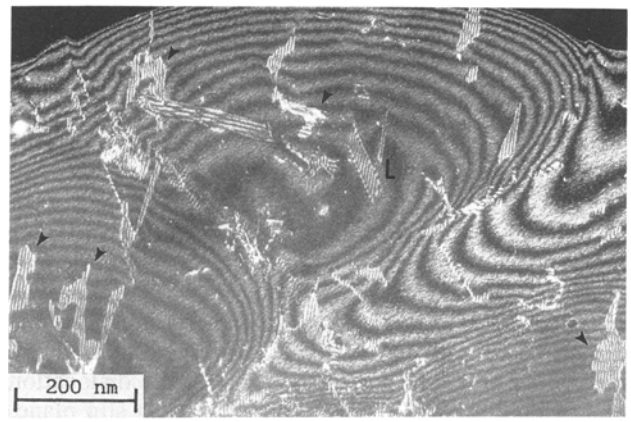

(b)

Fig. 5—Substructure after 20 cycles of fully reversed deformation at 200 °C, $\Delta\gamma_p = 0.10$ pct, $\dot{\varepsilon} = 50$ pct/min: (*a*) weak-beam **g**-3**g** $\langle 200\rangle$ micrograph showing faulted loops in the precipitates (marked by L) and faults in the matrix (marked by M); (*b*) weak-beam **g**-3**g** $\langle 200\rangle$ micrograph from a different area showing a faulted loop exhibiting a ribbon of fault along its perimeter (marked by L) and many asymmetric faults which appear to be pinned (marked by arrows).

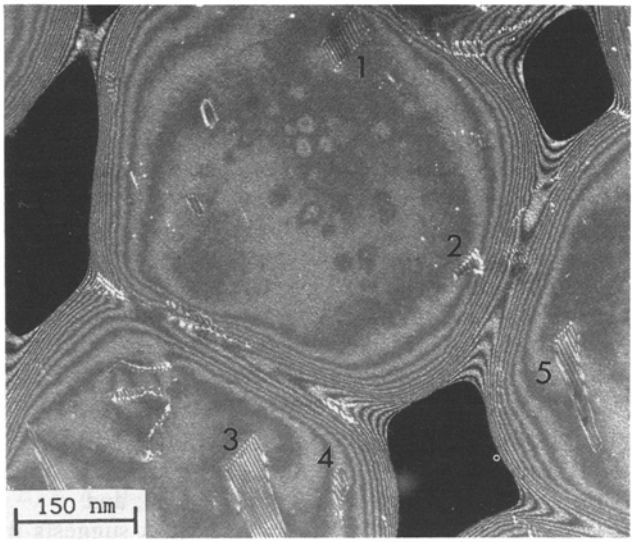

(*a*)

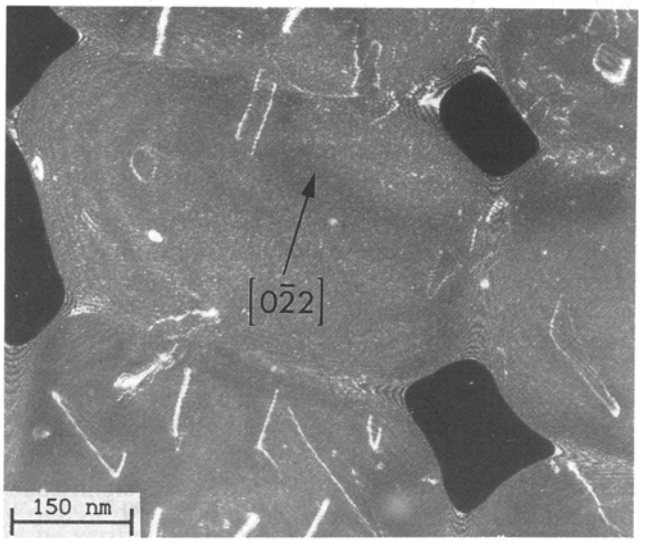

(*b*)

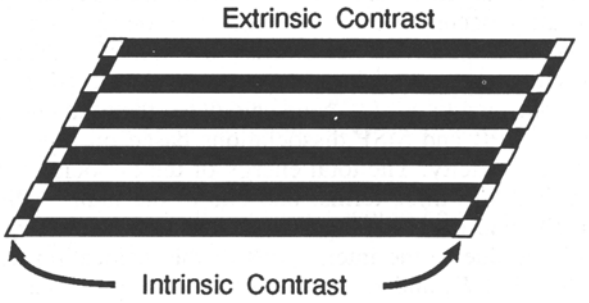

(*c*)

Fig. 6—Substructure after 6 cycles of fully reversed deformation at 20 °C, $\Delta\gamma_p$ = 0.11 pct, $\dot{\varepsilon}$ = 50 pct/min: (*a*) weak-beam **g**-3**g** [020] micrograph showing faulted SESF loops; (*b*) same area, weak-beam **g**-3**g** [0$\bar{2}$2] micrographs, showing (along with trace analysis) that many of the linear segments are nearly parallel to the Burgers vector of the primary octahedral glide dislocations; (*c*) schematic showing the type of contrast observed in faults 1 through 5 in (a), as well as fault L in Fig. 5(b).

Figure 6 shows two weak-beam images from a different foil which was deformed at 20 °C. The Burgers vectors of the two partials which bound the fault marked "1" are both parallel to [1$\bar{2}$1], and both the dislocations and the fault lie on (111). (The same is true of the fault marked "2.") This indicates that the faults are not bounded by a pair of dislocations but by a dislocation loop which has been intersected by both the top and bottom of the foil. The faults are SESFs. Inspection of fault 1 and the faulted loops marked "3," "4," and "5," as well as the faulted loop marked "L" in Figure 5(b), reveals a thin ribbon of fault around the perimeter of the major fault. This ribbon exhibits fringe contrast which is opposite in sign to the main fault, as shown schematically in Figure 6(c). This contrast indicates that the SESF is actually two closely spaced, parallel SISFs. (However, it was not possible to resolve the individual $a/3\langle 112\rangle$ partials which should be present in this configuration.) Figure 7 shows a heavily faulted area of a different foil that exhibits both stacking fault contrast and residual fault contrast on the same slip plane. The residual contrast is produced by three superimposed SISFs, which as a group have a value of $R_f = a\langle 111\rangle$ and, therefore, will not produce strong diffraction contrast.

Figure 6(b) illustrates an interesting feature of the deformation structures. Often, faults are bounded by linear partial dislocations which appear to be sessile. Figure 6(b), along with a rigorous trace analysis, revealed that these linear segments are parallel to [0$\bar{1}$1], which is the Burgers vector of the primary octahedral dislocations in this crystal. Note also that the loops 1, 2, 3, and 5 are asymmetric, with long segments nearly parallel to [0$\bar{1}$1]. These linear segments are parallel to screw dislocations in the primary [0$\bar{1}$1](111) system. Figure 6(b) is representative of the entire foil, which contained many linear segments parallel to [0$\bar{1}$1]. This configuration is discussed later.

2. *Temperature dependence of low-T faults*

The low-T faults were observed in every foil which was prepared from material cyclically deformed at 20 °C. As reported previously by the authors[3] and as seen in Figure 5, faults were also observed after deformation at 200 °C. Qualitatively, the density of faults observed after deformation at 200 °C appeared to be lower

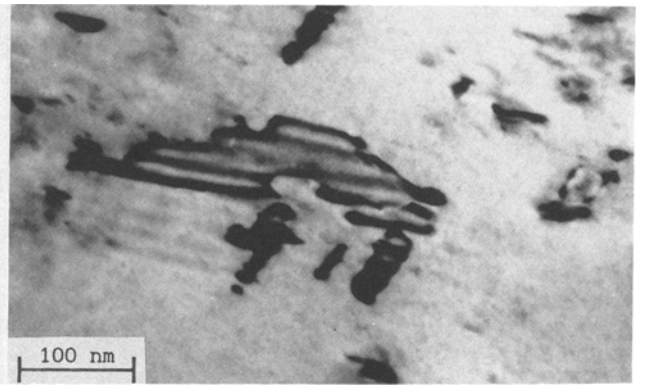

Fig. 7—Bright-field micrograph showing residual fault contrast, indicative of three overlapping SISFs, after 300 cycles of fully reversed deformation at 20 °C, $\Delta\gamma_p$ = 0.06 pct, $\dot{\varepsilon}$ = 50 pct/min, **g** = $\langle 111\rangle$, w = 0.

than after deformation at 20 °C. However, after deformation at 400 °C and 600 °C, very few faults were observed, as typified by Figure 8. The substructure consists mainly of matrix and interfacial dislocations, along with nearly screw $\{111\}a\langle 110\rangle$ dislocations within the γ'.

IV. DISCUSSION

A. *The Mechanism of Low-T SISF Formation*

Given the available experimental observations, the mechanism of SISF formation at temperatures below 400 °C cannot be determined beyond reasonable doubt. Although dislocation pairs consistent with an $a\langle 110\rangle$ decomposition (*via* Reaction [2]) were occasionally observed, they were always present in heavily faulted areas and in close proximity to other faults and partials. They could have been produced by dissociations involving more than one dislocation. The most common feature in the deformation substructures was the faulted loop, which was almost certainly produced as deformation debris, left behind by mobile glide dislocations that do not remain trapped within the γ'.

The deformation structures presented in this article are remarkably similar to those observed in several single-phase $L1_2$ materials strained at similar homologous temperatures. In Ni_3Ga deformed at ambient temperatures, the most common defect observed is a truncated SISF loop.[8,9] High densities of truncated SISF loops have been observed in Ni_3Al deformed below 350 °C.[10] Several investigators[8–11] have postulated that these SISF loops were produced as deformation debris by a mechanism similar to that proposed in Figure 4. This mechanism requires the dissociation of unit $a\langle 110\rangle$ superdislocations *via* Reaction [2], a dissociation which has been observed after low-temperature deformation of Ni_3Al,[10,12] Ni_3Ga,[11] Zr_3Al,[13,14] and Co_3Ti.[15] These studies, together with the analysis of the deformation debris presented in this article, suggest that the faulted loops observed in PWA 1480 after low-temperature deformation were produced by the mechanism illustrated in Figure 4.

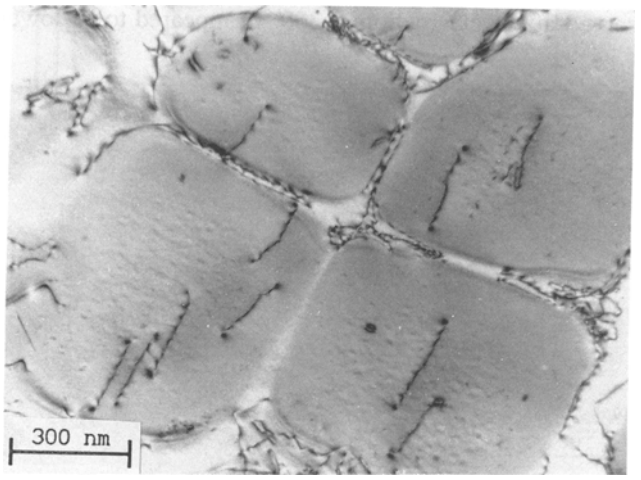

Fig. 8—Bright-field micrograph showing typical substructures, which do not contain stacking faults, after deformation at 400 °C. Fifty-two cycles of fully reversed deformation at 400 °C, $\Delta\gamma_p = 0.05$ pct, $\dot{\epsilon} =$ 50 pct/min, $\mathbf{g} = \langle 200\rangle$.

One other deformation mechanism which can produce SISF loops as debris has been observed by Veyssière *et al.*[16] in Ni_3Al deformed below 350 °C. As discussed earlier, when Ni_3Al is sheared by $a/2\langle 110\rangle$ pairs connected by an APB, the trailing partial can dissociate *via* Reaction [3], and an SISF loop can be left behind if the $a/3\langle 112\rangle$ partial becomes pinned. Veyssière *et al.* have called the structure a "faulted flag," due to the appearance of the faults being dragged behind the dislocations.[16] Since we have only observed the debris after deformation and not the reactant dislocations, this mechanism cannot be dismissed. However, circumstantial evidence suggests that this was not the primary deformation mechanism in the superalloy, since

(1) the structures observed in this study were qualitatively very similar to those discussed above,[8–15] which were not produced by the flag mechanism; and
(2) the observation of faults in the matrix suggests the existence of mobile $a/3\langle 112\rangle$ partials which do not always recombine after shearing the particle. This is more consistent with a pair of glissile $a/3\langle 112\rangle$ partials than with an APB pair which is dragging an SISF flag.

Therefore, it seems probable that the faulted loops observed in PWA 1480 after low-temperature deformation were formed by the mechanism proposed in Figure 4.

B. *The Temperature Dependence of Low-T SISF Formation*

Faulted loops have been observed after deformation at 200 °C and below in the superalloy. A similar temperature dependence of SISF formation has been observed in single-phase $L1_2$ materials as well. Veyssière *et al.*[16,17] have observed large faulted loops in Ni_3Al deformed at 20 °C but not at 350 °C. Takeuchi *et al.*[8] found a high density of SISFs in Ni_3Ga deformed at 20 °C but not at 400 °C. Finally, Holdway and Staton-Bevan[14] observed a high density of SISFs in Zr_3Al alloys deformed at low temperatures, but the density of SISFs was significantly reduced in the temperature range from 400 °C to 600 °C (depending on the alloy). Therefore, this temperature-dependent fault formation in the low-T regime is not limited to PWA 1480.

If one assumes that the $a\langle 110\rangle$ superdislocation dissociation occurs by Reaction [1], Reaction [2], or a combination of the two, a model exists which may be extended to study the temperature dependence of the SISF formation. Suzuki *et al.*[9] have calculated the total energies of the APB and SISF dissociations based on linear isotropic elasticity. The total energy of the dissociated system includes three terms: one due to the fault (APB or SISF), one due to the partial dislocation self energies, and one due to the interactions of the dislocation strain fields. Let E_a and E_s be the total energies of the APB and SISF dissociations, respectively, per unit length. Then,[9]

$$E_a = \Gamma_a d_a + \frac{\xi_1 \mu \mathbf{b}_a^2}{2\pi} \ln\left[\frac{R}{r_a}\right] - \frac{\xi_1 \mu \mathbf{b}_a^2}{2\pi} \ln\left[\frac{d_a}{R}\right] \quad [4]$$

and

$$E_s = \Gamma_s d_s + \frac{\xi_2 \mu \mathbf{b}_s^2}{2\pi} \ln\left[\frac{R}{r_s}\right] - \frac{\xi_3 \mu \mathbf{b}_s^2}{2\pi} \ln\left[\frac{d_s}{R}\right] \quad [5]$$

where Γ = fault energy;
d = equilibrium partial dislocation spacing;
μ = shear modulus;
$\mathbf{b}$ = Burgers vector ($\mathbf{b}_a = a/\sqrt{2}$ and $\mathbf{b}_s = a\sqrt{2}/3$);
r = dislocation core radius;
R = dislocation outer cutoff radius; and
ξ_i = geometric (dislocation character) terms.

Equation [4] may be subtracted from Eq. [5] to determine which dissociation scheme is favorable. After substituting reasonable values for the microstructural parameters and simplifying, the following criteria are obtained for the limiting cases of edge and screw $a\langle 110\rangle$ precursor dislocations:[9]

$$E_s < E_a \text{ if } \frac{\Gamma_a^2}{\Gamma_s} \gtrsim \frac{\mu \mathbf{b}_a}{\pi} \quad \text{(screw precursor)} \qquad [6]$$

$$\frac{\Gamma_a^{9/7}}{\Gamma_s} \gtrsim \left[\frac{\mu \mathbf{b}_a}{\pi}\right]^{2/7} \quad \text{(edge precursor)}$$

Substituting representative material parameters for Ni_3Al at room temperature (μ = 90 GPa,[18] $\mathbf{b} = 2.5 \times 10^{-10}$ m, and the fault energies[18–22] Γ_a = 110 mJ/m^2 and Γ_s = 10 mJ/m^2), it is found that the SISF dissociation is favored for edge dislocations and the APB dissociation is favored for screw dislocations. Therefore, one expects to find a mixture of APB-dissociated and SISF-dissociated dislocations after room-temperature deformation, as is observed.

The variation in shear modulus is small in the temperature range from 20 °C to 400 °C, so the temperature dependence of the dissociation may be explained by the temperature dependence of the fault energy ratios, Γ_a^x/Γ_s. Under the present set of assumptions, if the fault energy ratio decreases as the temperature increases from 20 °C to 400 °C, the density of SISFs should decrease and the density of APB pairs should increase. This is consistent with the experimental observations, but the model cannot be verified without a knowledge of the temperature dependence of the fault energies. It is frequently assumed (though often debated[23,24]) that the APB energy of Ni_3Al is nearly constant from room temperature to about 700 °C,[16,19,23–27] which implies that the fault energy ratio decreases with temperature from 20 °C to 400 °C because the SISF energy increases. This is consistent with the fact that the stacking fault energy of many disordered face-centered cubic (fcc) materials increases by about a factor of 2 as the temperature increases from zero to 350 °C.[28,29] High-temperature, *in situ* measurements of APB and SISF energies would be most helpful in verifying these suggestions.

C. *The Fault Configurations*

It is surprising that 90 pct of the stacking faults analyzed after low-temperature deformation were SESFs. However, as already stated, it appears that the SESFs were formed by $a/3\langle 112\rangle$ SISF glide on closely spaced parallel slip planes. This is supported by the occurrence of overlapping faults, as typified by Figures 3 and 7. Also, slip traces observed on the specimen surface grew by a mechanism similar to Lüders bands, starting as fine slip traces and expanding into a band as deformation proceeded.[4] This suggests that deformation may have occurred *via* a double cross-slip mechanism and would explain the closely spaced slipbands and overlapping faults presented in this study.

The occurrence of extrinsic faults and overlapping faults can be better understood with the aid of Figure 9 and the discussion in the Appendix. Assume that an SISF loop had been left behind in a γ' precipitate by the mechanism proposed in Figure 4. A simple calculation shows that the strain fields of the $a/3[\bar{1}\bar{1}2]$ partial and the $a[\bar{1}01]$ dislocation are repulsive; also, any reaction between the $a/3[\bar{1}\bar{1}2]$ and the $a[\bar{1}01]$ (or its leading superlattice partials, either $a/2[\bar{1}01]$ or $a/3[\bar{2}11]$) will result in an increase in energy (by Frank's rule) without eliminating an SISF. Thus, the faulted loop acts as a strong obstacle to the $a[\bar{1}01]$ dislocations which follow in the same slipband (Figure 9(a)). Inside the precipitate, a screw-oriented $a[\bar{1}01]$ superdislocation (which may have been dissociated by either the APB mechanism or the SISF mechanism) can recombine and cross slip one or more atomic planes to avoid the obstacle (Figure 9(b)). Once the $a[\bar{1}01]$ dislocation has escaped the plane of the obstacle, it can recommence glide on the original (more highly stressed) slip plane. Now, the dislocation is free to dissociate after the double cross-slip event. If it has changed its elevation by only one atomic plane and if it dissociates by an APB scheme after cross slip, the result would be a complex fault consisting of an APB on top of an SISF (Figure 9(c)). As discussed in the Appendix, this configuration is physically and energetically similar to a CSF and should have a very high fault energy. If, however, the double cross-slipped superdislocation dissociates by an SISF scheme after cross slip, the result would be two superimposed SISFs. As discussed in the

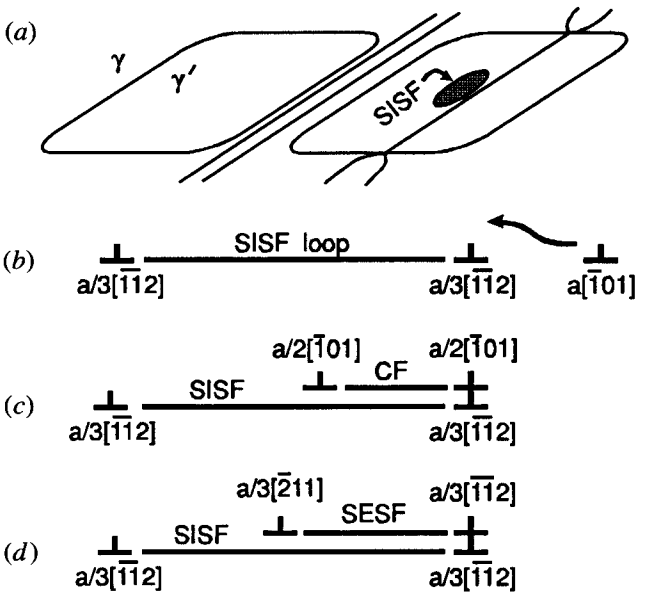

Fig. 9—Schematic diagram which shows possible multiplanar fault configurations when a screw-oriented $a\langle 110\rangle$ superdislocation encounters an SISF loop in its slip plane. Before constriction and cross slip, the $a\langle 110\rangle$ superdislocation may be dissociated by an APB or an SISF scheme. See Section IV–C for discussion.

Appendix, this is equivalent to an SESF (Figure 9(d)). Experimental observations suggest that an SESF has a lower energy than an SISF,[30] so the SESF should have a much lower energy than the complex fault shown in Figure 9(c). Therefore, the occurrence of an SISF loop on the slip plane promotes continued dissociation by the SISF scheme instead of the APB scheme, even though isolated screw superdislocations may be dissociated by an APB scheme. This explains the high density of SESFs and microtwins in the deformation structures.

Faults aligned along ⟨110⟩ directions have been observed previously in Ni_3Al[12,27] and Ni_3Ga.[8,9] Giamei *et al.*[12] have proposed that this arrangement is sessile and is obtained when the $a/3\langle 112\rangle$ partials dissociate into an $a/6\langle 112\rangle$ Shockley and an $a/2\langle 110\rangle$ partial on the {100} plane. Irrespective of whether or not this is the actual mechanism, the observed partials do appear to have a low mobility. Faulted SISF loops such as those observed in the present study should self-annihilate if the partial dislocations bounding the loops are glissile. For example, the truncated loop marked "1" in Figure 6 is bounded by dislocations of opposite sign, so there is an attractive elastic interaction in addition to the stacking fault, both of which should close the loop.

This sessile configuration (with elongated obstacles parallel to the Burgers vector of the primary glide dislocations) helps promote the multiple cross-slip mechanism shown in Figure 9. Glide dislocations which are not necessarily in the screw orientation are forced into the screw orientation when they encounter the faulted, elongated loops in their glide path. This aids the cross-slip process and results in the SESFs and the overlapping faults which are presented in this article.

V. SUMMARY

In PWA 1480 nickel-base superalloy single crystals, there are two temperature regimes in which superlattice stacking faults are produced by deformation. In the range from 700 °C to 950 °C, single isolated SISFs are produced by the decomposition of an $a/2\langle 110\rangle$ matrix dislocation in the γ/γ' interface. The $a/3\langle 112\rangle$ partial shears the particle, while the $a/6\langle 112\rangle$ Shockley remains in the interface, pinned by the high-energy APB which would be created if it entered the precipitate. At 200 °C and below, a high density of faults is produced on closely spaced, parallel planes. The most common feature after deformation in this range is the faulted loop, which is most often observed to be an SESF. These low-temperature faults, along with their temperature dependence, were quite similar to those observed in single-phase $L1_2$ materials. In contrast to the high-temperature faults, the available evidence strongly suggests that the low-temperature faults were produced by the dissociation of an $a\langle 110\rangle$ unit superdislocation into a pair of $a/3\langle 112\rangle$ partials. The temperature dependence of the faulting (at low temperatures) may be modeled by linear isotropic elasticity; results from this effort suggest that the SISF energy increases dramatically from 20 °C to 400 °C. *In situ* experiments would be most helpful in verifying these suggestions.

An analysis of multiplanar faults suggests that an APB on top of an SISF has a very high fault energy, similar to a CSF. Therefore, the presence of SISF loops on glide planes promotes further dissociation by the SISF scheme instead of the APB scheme and explains the high density of SESFs and microtwins in the deformation structures.

APPENDIX

Multiplanar faults

When analyzing multiplanar faults, such as those created by shear on parallel planes during this investigation, a convenient physical model is helpful. Such a model is presented in Figure A1. The figure shows the octahedral slip plane in the $L1_2$ lattice and indicates the positions of the Al and Ni atoms. Since each Al atom is surrounded only by Ni nearest neighbors, Al atoms always occupy sites designated by the script symbols. The $\mathscr{C}$ plane is in the plane of the paper, the $\mathscr{B}$ plane is below, and the $\mathscr{A}$ plane is above. The stacking sequence, considering an Al atom as the origin, is $\mathscr{ABC}/\mathscr{ABC}$, as shown in Figure A2.

Planar faults may be studied by determining the displacements of individual atoms after dislocation motion. For example, consider the Al atom which sits in the central $\mathscr{A}$ site in the perfect crystal (this would be a black atom sitting on top of the plane of the paper). The atomic displacements associated with the four fundamental slip vectors may be ascertained by studying Figure A1.

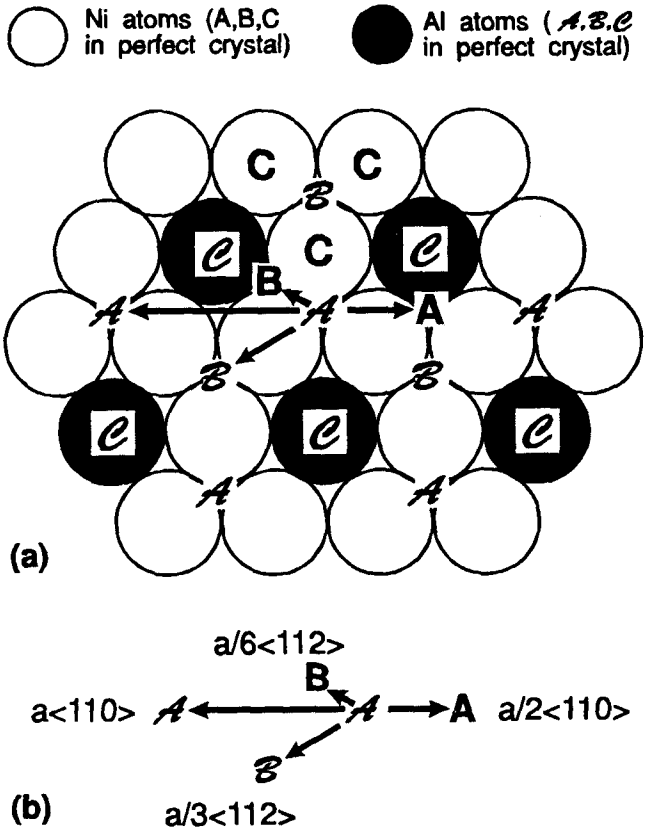

Fig. A1—Schematic diagram showing atomic positions and shear displacements in the $L1_2$ crystal structure. In the perfect crystal, Al atoms (filled circles in the diagram) always occupy the "script" sites. The $\mathscr{B}$ plane is below the paper; the $\mathscr{A}$ plane is above the paper.

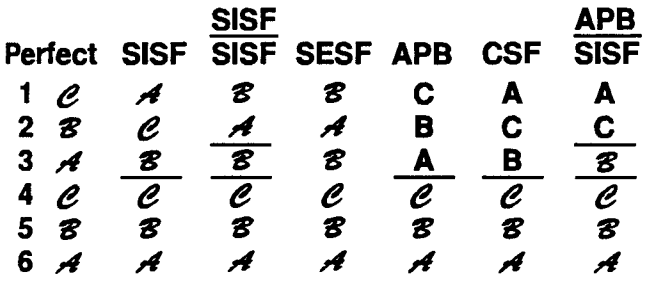

Fig. A2—Schematic diagram showing stacking sequences after various multiplanar shears of the $L1_2$ crystal structure. The diagram is prepared by observing an aluminum site in the perfect crystal (script symbols) and replacing script symbols with standard symbols when an Al atom is sheared into a Ni site.

Stacking sequences after slip may be constructed from these observations, and they are summarized in Figure A2.

For example, a nearest-neighbor APB is created by the $a/2\langle 110\rangle$ shear, which displaces the Al atom from $\mathcal{A}$ to A. Physically, this nearest-neighbor APB corresponds to two Al atoms touching one another (Figure A1). In the stacking sequence model of Figure A2, the nearest-neighbor APB is observed as an interface between the "script" sites and the "standard" sites, $\mathcal{ABC}$/ABC. As another example, an SISF is created by the $a/3\langle 112\rangle$ shear, which displaces the Al atom from $\mathcal{A}$ to $\mathcal{B}$. The Al atom is still surrounded by only Ni nearest neighbors, so no nearest-neighbor APB is present. As a third example, by imposing an $a/3\langle 112\rangle$ shear on parallel planes, the equivalence of an SESF and two parallel SISFs may also be readily deduced.

A more complicated problem which is relevant to the present investigation concerns the relative energies of the SESF, CSF, and APB/SISF configurations, as discussed in Section IV–C. As a first approximation, one may examine the first and second nearest-neighbor bond violations in each configuration with the aid of Figure A2. As an example, consider the atom sitting on the plane marked "3" in the vicinity of a CSF. The bond violations associated with atoms on this plane consist of a nearest-neighbor APB (B/$\mathcal{C}$), a second nearest-neighbor APB (B/$\mathcal{B}$), and second nearest-neighbor stacking fault (B/$\mathcal{B}$).

Table A1. Bond Violations across Several Planar Faults

Plane Number	SESF	CSF	APB over SISF
1	2NN SF ↓		2NN APB ↓
2			NN APB ↓
		2NN APB ↓	2NN APB ↓
		2NN SF ↓	2NN SF ↓
3		NN APB ↓	NN APB ↑
	2NN SF ↓	2NN APB ↓	2NN APB ↑
	2NN SF ↑	2NN SF ↓	2NN SF ↓
4		NN APB ↑	
		2NN APB ↑	2NN APB ↑
		2NN SF ↑	2NN SF ↑
5		2NN APB ↑	
	2NN SF ↑	2NN SF ↑	2NN SF ↑

Notes: Plane number corresponds to Fig. A2; NN = nearest neighbor; 2NN = second nearest neighbor; and the arrows refer to the direction of the bond violation with respect to Fig. A2.

Table A1 summarizes the bond violations (to the second nearest neighbor) for the two configurations which may result when an SISF loop blocks the slip plane (as well as for a CSF). It is found that the APB/SISF configuration [the CF in Figure 9(c)] has the same number of first and second nearest-neighbor violations as the CSF. Figure A2 shows that the stacking sequences are also quite similar. Therefore, it is reasonable to assume that the energy of an APB on top of an SISF is very high, similar to a CSF. It is clear from Table A1 that the SESF (or, equivalently, two superimposed SISFs) should have a much lower energy, as observed experimentally.[30]

ACKNOWLEDGMENTS

This research was sponsored by NASA-Lewis Research Center, under Grant NAG3-503, which was monitored by Dr. Robert C. Bill and Mr. Michael Verrilli. WWM acknowledges the Centre d' Etudes Nucléaires de Grenoble, France, for postdoctoral support during the latter stages of this work and for the use of the JEOL 2000FX. We thank Dr. Patrick Veyssière, of Centre National de la Recherche Scientifique-l'Office National d'Etudes et de Recherches Aérospatiales, Châtillon, France, for lively discussions, a domestic travel grant, and for the use of the JEOL 4000FX.

REFERENCES

1. W.W. Milligan and S.D. Antolovich: *Metall. Trans. A*, 1987, vol. 18A, pp. 85-95.
2. D.M. Shah and D.M. Duhl: in *Superalloys 1984, Proc. 5th Int. Symp. on Superalloys*, M. Gell, C.S. Kortovich, R.H. Bricknell, W.B. Kent, and J.F. Radavich, eds., AIME, Warrendale, PA, 1984, pp. 105-14.
3. W.W. Milligan and S.D. Antolovich: *Metall. Trans. A*, 1989, vol. 20A, pp. 1888-89.
4. W.W. Milligan and S.D. Antolovich: NASA CR-4215, Cleveland, OH, 1989.
5. P. Caron, T. Khan, and P. Veyssière: *Phil. Mag. A*, 1988, vol. 57, pp. 859-75.
6. R. Bonnet and A. Ati: *Acta Metall.*, 1989, vol. 37, pp. 2153-69.
7. M. Condat and B. Décamps: *Scripta Metall.*, 1987, vol. 21, pp. 607-12.
8. S. Takeuchi, E. Kuramoto, T. Yamamoto, and T. Taoka: *Jpn. J. Appl. Phys.*, 1973, vol. 12, pp. 1486-92.
9. K. Suzuki, M. Ichihara, and S. Takeuchi: *Acta Metall.*, 1979, vol. 27, pp. 193-200.
10. I. Baker and E.M. Schulson: *Phys. Status Solidi*, 1985, vol. 89, pp. 163-72.
11. H-r. Pak, T. Saburi, and S. Nenno: *Scripta Metall.*, 1976, vol. 10, pp. 1081-85.
12. A.F. Giamei, J.M. Oblak, B.H. Kear, and W.H. Rand: *Proc. EMSA*, 1971, vol. 29, pp. 112-13.
13. L.M. Howe, M. Rainville, and E.M. Schulson: *J. Nucl. Mater.*, 1974, vol. 50, pp. 139-54.
14. P. Holdway and A.E. Staton-Bevan: *J. Mater. Sci.*, 1986, vol. 21, pp. 2843-49.
15. Y. Liu, T. Takasugi, O. Izumi, and T. Takahashi: *Acta Metall.*, 1988, vol. 36, pp. 2959-66.
16. P. Veyssière, J. Douin, and P. Beauchamp: *Phil. Mag. A*, 1985, vol. 51, pp. 469-83.
17. P. Veyssière, D.L. Guan, and J. Rabier: *Phil. Mag. A*, 1984, vol. 49, pp. 45-54.
18. M.H. Yoo: *Scripta Metall.*, 1986, vol. 20, pp. 915-20.
19. M.H. Yoo: *Acta Metall.*, 1987, vol. 35, pp. 1559-70.
20. G. Vanderschaave: *Phil. Mag. A*, 1987, vol. 56, pp. 689-701.
21. J. Douin, P. Veyssière, and P. Beauchamp: *Phil. Mag. A*, 1986, vol. 54, pp. 375-93.
22. V. Vitek: *Phil. Mag. A*, 1988, vol. 58, pp. 193-212.

23. J.K. Tien, S. Eng, and J.M. Sanchez: *MRS Proc.*, 1987, vol. 81, pp. 183-93.
24. J.M. Sanchez, S. Eng, Y.P. Yu, and J.K. Tien: *MRS Proc.*, 1987, vol. 81, pp. 57-64.
25. S.M. Copley and B.H. Kear: *Trans. TMS-AIME*, 1967, vol. 239, pp. 984-92.
26. P.A. Flinn: *Trans. TMS-AIME*, 1960, vol. 218, pp. 145-54.
27. I. Baker and E.M. Schulson: *Phys. Status Solidi A*, 1984, vol. 85, pp. 481-90.
28. L. Remy, B. Thomas, and A. Pineau: *Mater. Sci. Eng.*, 1978, vol. 36, pp. 47-63.
29. P.C.J. Gallagher: *Metall. Trans.*, 1970, vol. 1, pp. 2429-61.
30. G.S. Hillier, C.M.F. Rae, and H.K.D.H. Bhadeshia: *Acta Metall.*, 1988, vol. 36, pp. 95-109.